PLOS ONE

RESEARCH ARTICLE

The structural basis of a high affinity ATP binding ε subunit from a bacterial ATP synthase

Alexander Krah[1,2]*, **Yasuyuki Kato-Yamada**[3], **Shoji Takada**[1]

1 Department of Biophysics, Graduate School of Science, Kyoto University, Kitashirakawa-Oiwakecho, Sakyo-ku, Kyoto, Japan, **2** School of Computational Sciences, Korea Institute for Advanced Study, Dongdaemun-gu, Seoul, Republic of Korea, **3** Department of Life Science, College of Science, Rikkyo University, Nishi-Ikebukuro, Toshima-ku, Tokyo, Japan

* alexkrah@kias.re.kr

Check for updates

OPEN ACCESS

Citation: Krah A, Kato-Yamada Y, Takada S (2017) The structural basis of a high affinity ATP binding ε subunit from a bacterial ATP synthase. PLoS ONE 12(5): e0177907. https://doi.org/10.1371/journal.pone.0177907

Editor: Hendrik W. van Veen, University of Cambridge, UNITED KINGDOM

Received: December 1, 2016

Accepted: May 4, 2017

Published: May 18, 2017

Copyright: © 2017 Krah et al. This is an open access article distributed under the terms of the Creative Commons Attribution License, which permits unrestricted use, distribution, and reproduction in any medium, provided the original author and source are credited.

Data Availability Statement: All relevant data are within the paper and its Supporting Information files.

Funding: AK was supported by a Postdoctoral Fellowship for Foreign Researchers from the Japan Society for the Promotion of Science (JSPS-ID: P13705) (https://www.jsps.go.jp/). Computational resources have been provided by the Okazaki Research Centre for Computational Sciences (to ST; https://ccportal.ims.ac.jp/en/). Part of this work was supported by JSPS KAKENHI (15K07013 to YKY). The funders had no role in study design, data

Abstract

The ε subunit from bacterial ATP synthases functions as an ATP sensor, preventing ATPase activity when the ATP concentration in bacterial cells crosses a certain threshold. The R103A/R115A double mutant of the ε subunit from thermophilic *Bacillus* PS3 has been shown to bind ATP two orders of magnitude stronger than the wild type protein. We use molecular dynamics simulations and free energy calculations to derive the structural basis of the high affinity ATP binding to the R103A/R115A double mutant. Our results suggest that the double mutant is stabilized by an enhanced hydrogen-bond network and fewer repulsive contacts in the ligand binding site. The inferred structural basis of the high affinity mutant may help to design novel nucleotide sensors based on the ε subunit from bacterial ATP synthases.

Introduction

ATP synthases, the universal energy conversion machinery in all living cells, synthesize ATP by a rotational motion [1], inducing the catalytic reaction of synthesizing ATP by phosphorylating ADP. This rotational motion is induced by an electrochemical proton [2] or sodium ion [3] gradient; the molecular and energetic basis for the ion selectivity have been characterized previously [4]. Vice versa, under certain cellular conditions, ATP hydrolysis can be induced to maintain the electrochemical gradient, rotating in the opposite direction [5]. To prevent the waste of ATP, ATPase activity in bacteria and mammals is supressed by common and distinct regulatory mechanisms. The common ATPase inhibition mechanism in mammals [6] and bacteria [7] is MgADP inhibition [8]. Additionally the mammalian ATP synthase is regulated by IF_1 [9], sensing the pH in the cell. If the pH drops below 6.5 [10], the IF_1 tetramer [11] splits into two dimers and inhibits two ATP synthases simultaneously [12]. The ATPase activity in bacterial cells is regulated by the ε subunit, sensing the ATP concentration. A large conformational change from the non-inhibitory down- to the inhibitory up-state is induced, if the ATP

collection and analysis, decision to publish, or preparation of the manuscript.

Competing interests: The authors have declared that no competing interests exist.

concentration passes a certain threshold [13–15]. This transition inhibits ATP hydrolysis activity by binding to the catalytic $\alpha_3\beta_3$ subunit assembly [16–18], slowing down hydrolysis and synthesis reactions by supressing substrate binding and product release [19]. A recent review on the different regulatory mechanism of bacterial and mammalian ATP synthases can be found elsewhere [20].

For the first time it was shown in 2003 that the isolated ε subunit from thermophilic *Bacillus* PS3 binds ATP [21]. The ATP threshold of the ε subunit from bacterial ATP synthases is found from the μM (4.3 μM) in the wild type ε subunit from thermophilic *Bacillus* PS3 [22] to the mM range in the wild type ε subunit from *Bacillus subtilis* (2.1 mM) [23] or *Escherichia coli* (22 mM) [24]. The decrease in the binding affinities of the latter relative to the ε subunit from thermophilic *Bacillus* PS3 may be caused by different ATP binding residues [25] and an allosteric Mg^{2+} binding site [26] for *Escherichia coli* and *Bacillus subtilis*, respectively. Indeed, it has been shown that alanine mutations of residues located in the binding site in the ε subunit from thermophilic *Bacillus* PS3 decrease the binding affinity [22]. Surprisingly, however, the introduction of the R103A/R115A double mutation into the ε subunit from thermophilic *Bacillus* PS3 increases the binding affinity of ATP by two orders of magnitude [27]. Despite available biochemical data for some organisms, structural data clarifying the different ATP binding strengths of the ε subunit from these organisms is hardly available. The ε subunit from *Thermosynechococcus elongates* BP-1 could be resolved by NMR spectroscopy [28] and the structural basis of the ε subunit from *Escherichia coli* could be elucidated by NMR spectroscopy [29] and X-ray crystallography [25]. These structures are obtained for the isolated subunit in the down-state not being bound to ATP. In addition, crystal structures of the isolated ε subunit from thermophilic *Bacillus* PS3 [24] could give first insights into ATP binding to subunit ε. A theoretical study on the ε subunit from thermophilic *Bacillus* PS3 [30] could identify that Mg^{2+} is bound to ATP:Oα/Oβ, being confirmed recently by the structure of the ε subunit from *Caldalkalibacillus thermarum* [31]; the corresponding ATP binding site of the ε subunit from *Caldalkalibacillus thermarum* is shown in S1 Fig.

Based on the ε subunit from bacterial ATP synthases, ATP sensor proteins [32–34] have been developed recently and applied to understand biological functions for several organisms as mammals [35], plants [36], bacteria [33] and cells infected by a virus [37]. The R103A/R115A double mutant therefore has the potential to further extend the range of measuring ATP concentrations in a low concentration range, as e.g. for changes of extracellular ATP levels, important for signal transduction.

Here, we infer the structural basis of the ATP binding site of the R103A/R115A double mutant of the ε subunit from thermophilic *Bacillus* PS3, using molecular dynamics simulations and free energy calculations. In the double mutant, we observe a different binding site structure from what we have previously obtained for the wild type protein [30]. In the double mutant, an enhanced hydrogen bond network is observed and repulsive interactions between ligand coordinating residues themselves and the Mg^{2+} ion are reduced. Clarifying the structural basis of the R103A/R115A mutant, may allow to introduce additional site-directed mutations to design novel nucleotide sensors, as e.g. ADP or AMP sensors, based on the ε subunit from thermophilic *Bacillus* PS3. These sensors might be helpful to monitor the AMP/ADP concentrations to derive additional information about signalling pathways or the role of relevant proteins in diseases as e.g. the platelet ADP receptor [38] or adenosine monophosphate-activated protein kinase (AMPK) [39].

Material and methods

Conventional molecular dynamics simulations

Conventional MD simulations were carried out for the R103A/R115A mutant from the ε subunit from thermophilic *Bacillus* PS3 for three different sets. Starting structures for this runs were obtained from our previous (wild type) simulation after a total simulation time without any restraints (production) of 150 ns [30], followed by introduction of the mutations (R103A and R115A), thus we already used an equilibrated structure as an input; in this initial model no Mg^{2+} ion was bound to ATP. These systems were simulated for 150 ns; four Mg^{2+} ions were freely distributed in the bulk. In the second and third set of simulations, the final structures of the initial simulation (Mg^{2+} freely distributed) were taken as the starting structure for each individual run; one Mg^{2+} ion was modelled in a first sphere coordination to ATP:Oα/Oβ or ATP:Oβ/Oγ, respectively. The whole system and all three setups, denoting a different Mg^{2+} coordination states, are shown in Fig 1, highlighting the ligands (ATP and Mg^{2+}) and the

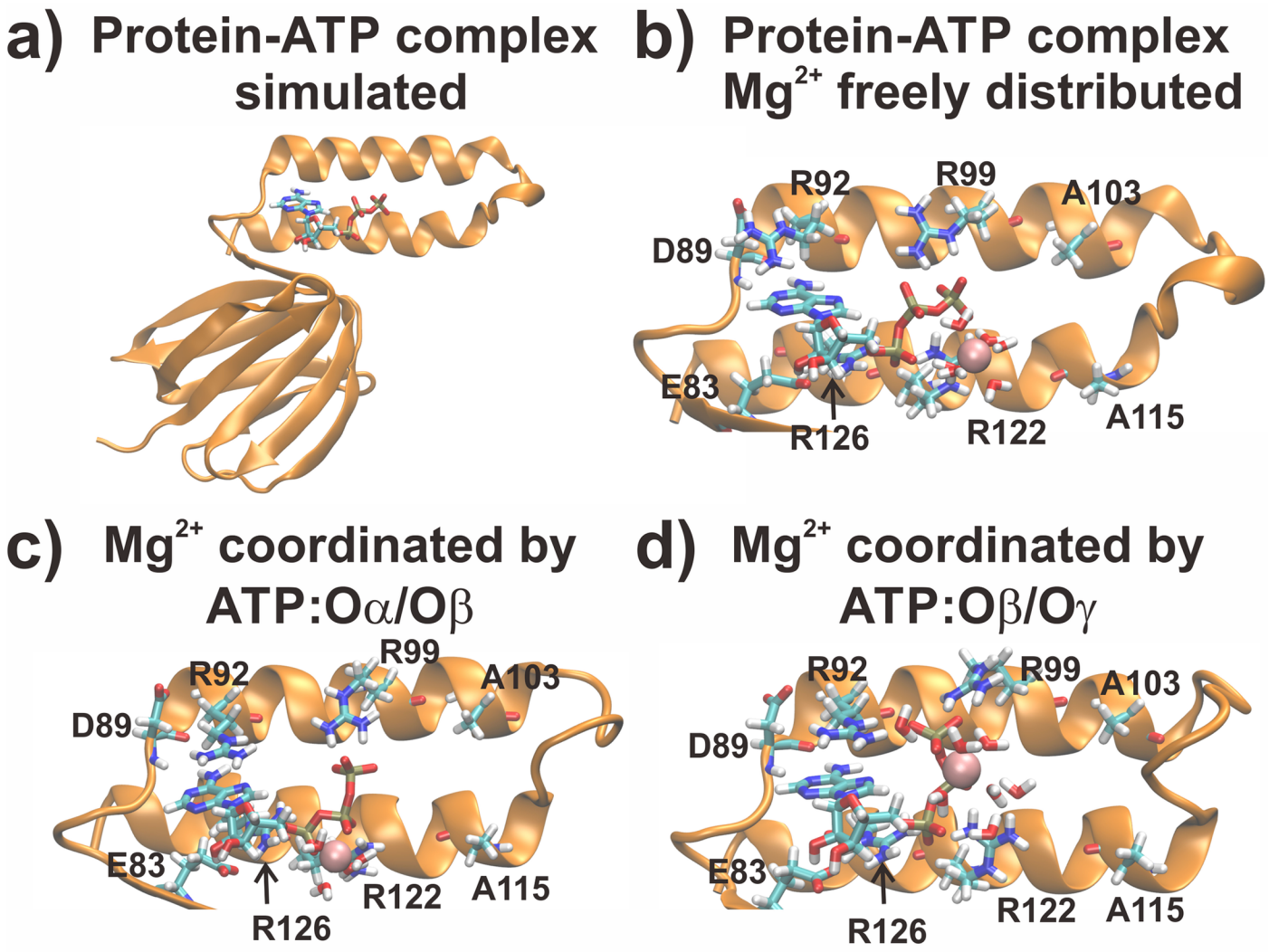

Fig 1. Input structures for the simulations. In a) the whole protein-ATP complex is shown. In b-d) the initial binding site structures for the freely distributed Mg^{2+} case, the MgATP:Oα/Oβ and MgATP:Oβ/Oγ coordination are shown, respectively. Water molecules coordinating the Mg^{2+} ion and residues coordinating ATP are shown in licorice, while the Mg^{2+} ion is shown in VdW spheres.

https://doi.org/10.1371/journal.pone.0177907.g001

binding site. The remaining three Mg^{2+} ions were freely distributed in the simulation system. These simulations were carried out for 100 ns. Three independent replicas were simulated for each system. We added counter ions to neutralize the simulation systems for all runs.

Simulations were carried out with the MD program GROMACS (version 4.6.5) [40], using the AMBER-ILDN force field [41–45], which has been implemented in GROMACS previously [46]. Mg^{2+} ion parameters were utilized as reported previously [47]. To keep pressure and temperature constant at 1 bar and 300 K, we used the Parrinello-Rahman barostat [48] and the velocity rescale thermostat [49]. Electrostatic interactions were calculated using a real space cut-off of 12 Å by the Particle Mesh Ewald method (PME) [50]. Van der Waals interactions were calculated using the same cut-off distance. An integration time step of 2 fs was used.

Free energy calculations

To clarify the Mg^{2+} coordination sphere, we calculated the solvation free energy of an Mg^{2+} ion in a second sphere coordination (the ATP phosphate group and the Mg^{2+} ion are bound via bridging water molecules) and in two possible first sphere coordination states (Mg^{2+} is bound to either ATP:Oα/Oβ or ATP:Oβ/Oγ). The different ion coordination states by ATP are shown in Fig 1 (Fig 1b: Mg^{2+} is shown in a second sphere coordination towards ATP, c: Mg^{2+} coordinated by ATP:Oα/Oβ and d: Mg^{2+} coordinated by ATP:Oβ/Oγ, respectively). We removed all Mg^{2+} ions, not being present in the sphere of interest (not the ones bound in the second sphere or bound to ATP in a first sphere, but the remaining three ions) to exclude any attractive effects of ATP to any of these Mg^{2+} ions (other than the bound one). The thermodynamic integration (TI) method was applied. We increased the coupling factor λ incrementally, using 85 windows. Van der Waals and electrostatic interactions were removed serially without using a soft-core potential. A restraint of 1.5 kcal/(mol*Å^2) was introduced to keep the ion in the designated position (relative position restraints of the Mg^{2+} ion to the ATP phosphate group). Forward and backward simulations were carried out for 500 ps per window, using the first 100 ps as equilibration time. Analysis of the results was carried out using the Bennet Acceptance Ratio (BAR) method [51] with the g_bar module as implemented in GROMACS. The standard deviation was derived on the basis of forward and backward direction of the TI calculations.

MM-PBSA calculations

Molecular Mechanics–Poisson Boltzmann Surface Area (MM-PBSA) calculations [52] were carried out with the program g_mmpbsa [53]. The electrostatic potential was calculated via APBS [54]. The ε subunit (R103A/R115A double mutant) was assigned as the protein, while ATP, Mg^{2+} and the Mg^{2+}-coordinating water molecules were defined as the ligand. We used the non-linear Poisson Boltzmann method (NLPB) [55]. The dielectric constant for the solute was set to ε = 2 and for the solvent ε = 80. A physiological NaCl concentration (150 mM) was added for the calculations. After an equilibration time of 10 ns, we analysed 900 snapshots of the remaining 90 ns per run and coordination state, skipping every 100 ps.

Additional analysis

To additionally explain the experimental results, we analysed the hydrogen bond network of the protein towards ATP and the protein-protein network between the second α-helical C-terminal domain, ranging from residue 112 to residue 133, with the remaining protein, using a cut-off distance of 2.7 Å from the donor hydrogen atom to the acceptor atom and a cut-off of 30° for the angle between donor hydrogen and acceptor atoms. Estimation of the energy

contribution of the hydrogen bond network, was estimated as proposed by Espinosa et al. [56]:

$$E_{HB} = -\frac{50}{2} * 10^3 * e^{(-3.6*d(H-O))} [kJ/mol]$$

where E_{HB} denotes the hydrogen binding energy and d(H-O) represents the distance between the donor hydrogen and the acceptor atom in Å.

To allow an initial equilibration of the system, we skipped the first 10 ns in this analysis. In addition, repulsive contacts were defined as contacts of positively charged residues located in the binding site and Mg^{2+} using a maximum distance of 4.5 Å. Standard deviations were calculated using the averages of all three runs.

Results

Recent experiments showed an unexpected binding affinity of ATP to the ε subunit of the R103A/R115A mutant from thermophilic *Bacillus* PS3. This double mutant binds ATP two orders of magnitude stronger (K_d = 52 nM) [27] than the wild type (K_d = 4.3 μM) [22] protein. Structural reasons for these different binding strengths of the ε subunit to ATP are not obvious. To understand these experimental results, we carried out conventional MD simulations for the R103A/R115A mutant of the ε subunit from thermophilic *Bacillus* PS3. As we have previously shown for the wild type ε subunit from thermophilic *Bacillus* PS3 [30], we observe a high probability of Mg^{2+} binding in a second sphere coordination (Fig 2a).

Compared to the wild type [30], we observe higher stability in the distance distributions if Mg^{2+} is freely distributed and not bound in a first sphere to ATP (S2 Fig). However, our previously conducted simulations obtained the presence of an Mg^{2+} bound to ATP, between atoms Oα and Oβ (in the first sphere coordination) [30]. Thus, we carried out additional conventional MD simulations, showing a stable Mg^{2+} ion coordination to ATP (Fig 2b and 2c). These simulations were followed by free energy calculations with an Mg^{2+} ion bound between Oα/Oβ and between Oβ/Oγ to derive the binding site composition. The free energy calculations show that the Mg^{2+} ion is bound to ATP in a first sphere coordination complex (Fig 2d)–to test if the results are converged, we analysed two additional time windows (100 ps– 300 ps and 300 ps to 500 ps per TI window); the results are shown in S3 Fig and indicate that the results derived by the solvation free energy calculations of the Mg^{2+} ion are converged. To further derive the binding mode of the Mg^{2+} ion, we analysed the obtained data with the MM-PBSA method [52]. The results indicate that the Mg^{2+} ion is bound to the ATP:Oα/Oβ atoms. The obtained average value for MgATP binding over all three runs is -27.9 +/- 0.8 kcal/mol for the ATP:Oα/Oβ and -25.4 +/- 4.2 kcal/mol for the ATP:Oβ/Oγ Mg^{2+} bound state. It should be noted that the MM-PBSA calculations failed to derive the energy differences and even the trend in respect to the wild type protein (-91.9 kcal/mol and -88.2 kcal/mol for the Mg^{2+} ion bound to ATP:Oα/Oβ and ATP:Oβ/Oγ, respectively [30]). However, a recent study claimed that the MM-PBSA method is capable to distinguish between similar ligands bound to the same protein [57]. The hydrogen bond analysis, as shown in Table 1a), also supports that the ion is coordinated by ATP:Oα/Oβ (instead of ATP:Oβ/Oγ). Converting our simulation results into hydrogen binding energy (E_{HB}), as introduced by Espinosa et al. [56], we obtained 99.8 +/- 1.8 kcal/mol and 95.1 +/- 2.6 kcal/mol for the Oα/Oβ and the Oβ/Oγ Mg^{2+} bound state, respectively, as it has been predicted previously for the wild type [30] and also has been shown by a current X-ray structure of the ε subunit from *Caldalkalibacillus thermarum* [31] (S1 Fig). The results are shown in Table 1b). These results are in agreement with the free energy calculations and the MM-PBSA calculations, thus we conclude that the Mg^{2+} ion is located between ATP:Oα/Oβ.

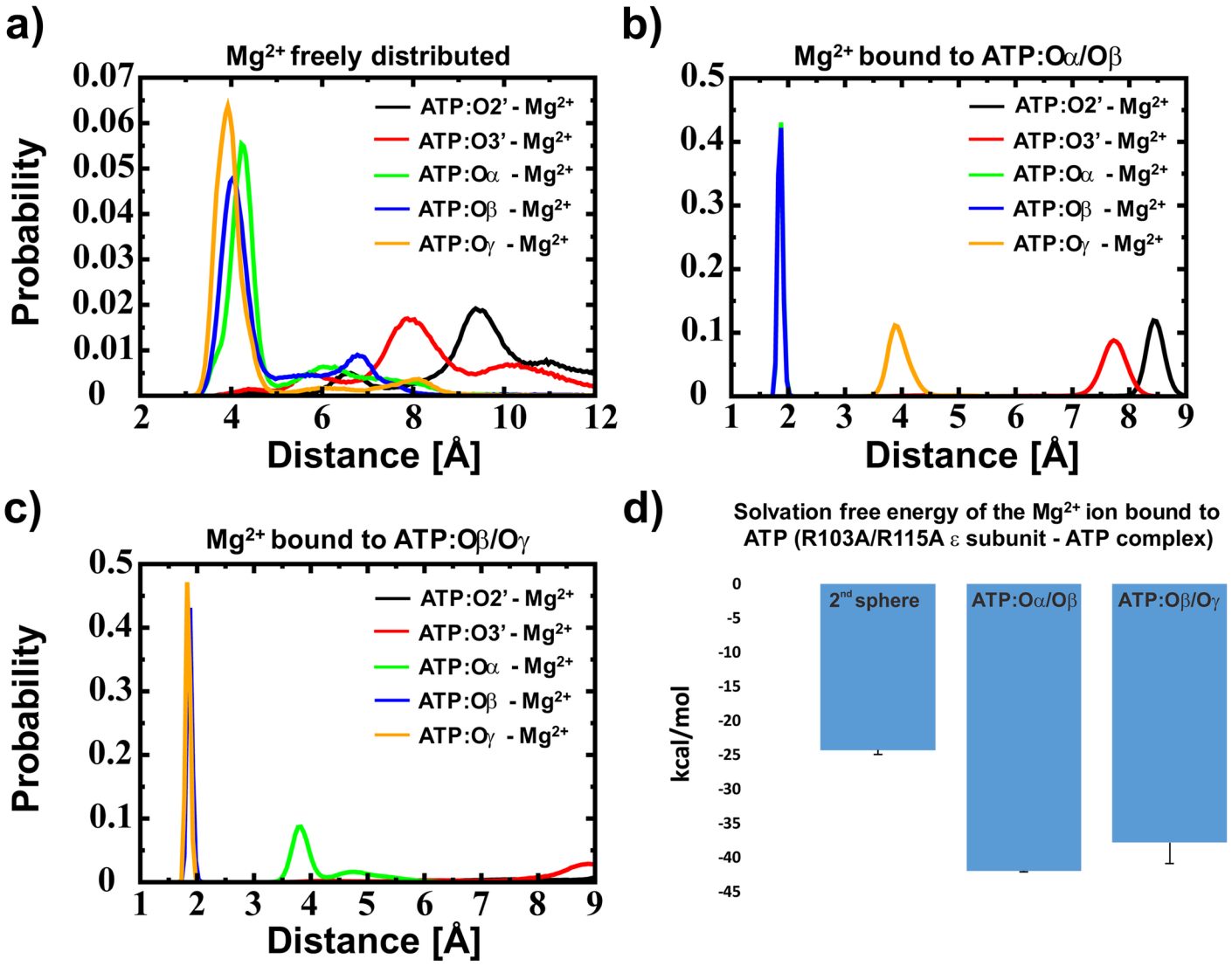

Fig 2. Distance distribution of the Mg^{2+} ion and free energy results. Distance distribution when the Mg^{2+} ion a) is bound in a second sphere coordination to ATP, b) is bound in a first sphere coordination to ATP:Oα/Oβ and c) is bound in a first sphere coordination to ATP:Oβ/Oγ; ATP is bound to the protein in all cases. In a)–c) the black, red, green, blue and orange lines represent the minimal distance distributions of a Mg^{2+} ion towards ATP:O2', ATP:O3', ATP:Oα, ATP:Oβ and ATP:Oγ, respectively. The before mentioned data were extracted from conventional MD simulations. In d) the free energy calculations (Thermodynamic Integration) for the binding of Mg^{2+} towards ATP in second sphere coordination, when bound to ATP:Oα/Oβ or ATP:Oβ/Oγ are shown, respectively. It should be noted that in Fig b) the blue and the green lines are overlapping.

https://doi.org/10.1371/journal.pone.0177907.g002

The nucleoside interactions are stable in our simulations as observed in the crystal structure. Additionally, ATP:Oα is coordinated by R126:NHx and R122:NHx, ATP:Oβ by flexible interactions of R122:NHx and R126:NHx and ATP:Oγ by R92:NHx, R92:Nε and R99:NHx (Fig 3). An Mg^{2+} ion is found to be coordinated by ATP:Oα/Oβ (Fig 2d). It should be noted that R99 and R122 are slightly displaced compared to the crystal structure, representing a more favourable hydrogen bond network. The binding sites of the wild type and the mutant ε subunit derived by molecular simulations are shown in Fig 4.

To understand the different binding strength of ATP binding towards the ε subunit of the wild type [22] and the R103A/R115A mutant [27] from thermophilic *Bacillus* PS3, we analysed the hydrogen bond network of the protein towards ATP, the internal protein-protein

Table 1. Hydrogen-bond and energetic analysis of ATP binding to the wild type and mutant ε subunit.

a)	Wild type (kcal/mol)		R103A/R115A (kcal/mol)	
	Oα/Oβ	Oβ/Oγ	Oα/Oβ	Oβ/Oγ
h-bonds (protein-ATP)	9.38 +/- 0.48	9.45 +/- 0.09	10.4 +/- 0.60	9.74 +/- 0.47
h-bonds (2^{nd} α-helix)	5.27 +/- 0.20	4.93 +/- 0.69	4.01 +/- 0.18	4.05 +/- 0.26
repulsive contacts	1.96 +/- 0.51	1.58 +/- 0.20	1.08 +/- 0.51	1.54 +/- 0.06
b)	Wild type (kcal/mol)		R103A/R115A (kcal/mol)	
	Oα/Oβ	Oβ/Oγ	Oα/Oβ	Oβ/Oγ
E_{HB} (h-bonds (protein-ATP))	64.6 +/- 2.4	65.2 +/- 0.1	73.4 +/- 2.1	67.8 +/- 2.9
E_{HB} (h-bonds (2^{nd} α-helix))	28.6 +/- 0.7	27.0 +/- 2.3	26.4 +/- 1.5	27.4 +/- 2.3
E_{HB}	93.2 +/- 0.31	92.2 +/- 0.42	99.8 +/- 1.8	95.2 +/- 2.6

a) The number of hydrogen bonds between the protein and ATP, internal protein-protein hydrogen bonds of the C-terminal second α-helix to the rest of the protein and repulsive contacts in the ε subunit from the wild type and the R103A/R115A mutant derived from MD simulations. b) Energetic analysis of the hydrogen bonding network towards ATP and the flexible α-helices. In a) and b) Oα/Oβ and Oβ/Oγ denote the ATP oxygen atoms to which the Mg^{2+} ion is coordinated during the simulation. Standard deviations were calculated using the averages of the three individual runs.

https://doi.org/10.1371/journal.pone.0177907.t001

hydrogen bond network and the repulsive contacts in the wild type and the R103A/R115A double mutant, respectively. The results are shown in Table 1. We observe an extended hydrogen binding network towards ATP in the mutant, while the hydrogen bonds between the flexible α-helix and the remaining residues are slightly reduced. To estimate the energy of hydrogen binding of MgATP to the ε subunit of thermophilic *Bacillus* PS3 (wild type and R103A/R115A mutant), we used an energy estimation based on the hydrogen binding network between the protein and the ligand [56]. Additionally, we estimated the hydrogen binding energy of the flexible α-helical domain, which undergoes the large conformational change from the down- to the up-state after ATP release. In total we calculate an energy penalty of 6.6 kcal/mol comparing the differences for the calculated hydrogen binding energy (Table 1b; $\Delta E_{HB} = E_{HB}(\text{mutant}) - E_{HB}(\text{wild type})$) of the wild type in respect to the R103A/R115A double mutant.

Discussion

In order to explain the increased ATP binding ability of the R103A/R115A mutant [27] in respect to the wild type ε subunit from thermophilic *Bacillus* PS3 [22], we carried out MD simulations of the R103A/R115A double mutant and compared these results with previously discussed ones of the wild type protein [30]. The ATP molecule, bound to the double mutant, binds a Mg^{2+} ion in the ATP:Oα/Oβ position, as we predicted for the wild-type; this Mg^{2+} position also could be shown by a current crystal structure of the F_1-complex from *Caldalkalibacillus thermarum* (PDB-ID: 5HKK), harbouring the ε subunit in the ATP bound down-state [31]; ATP is coordinated by homologous residues of subunit ε in this crystal structure [31] (S1 Fig). Our data show that the R103A/R115A mutant stabilizes ATP binding by an extended hydrogen-bond network between the protein and the ATP molecule and the flexible α-helical domain (Table 1) leading to an energy penalty of 6.6 kcal/mol of ATP binding in the wild type compared to the double mutant (Table 1). It should be noted that the E83:Oεx—ATP:O2' and protein-ATP:Oγ interactions are remarkably stabilized (Fig 3 top left—red line, bottom right and previous results [30]); the enhanced instability of this interaction in the wild type protein might be induced by attractive interactions of R103 and/or R115 with ATP:Oγ, causing a

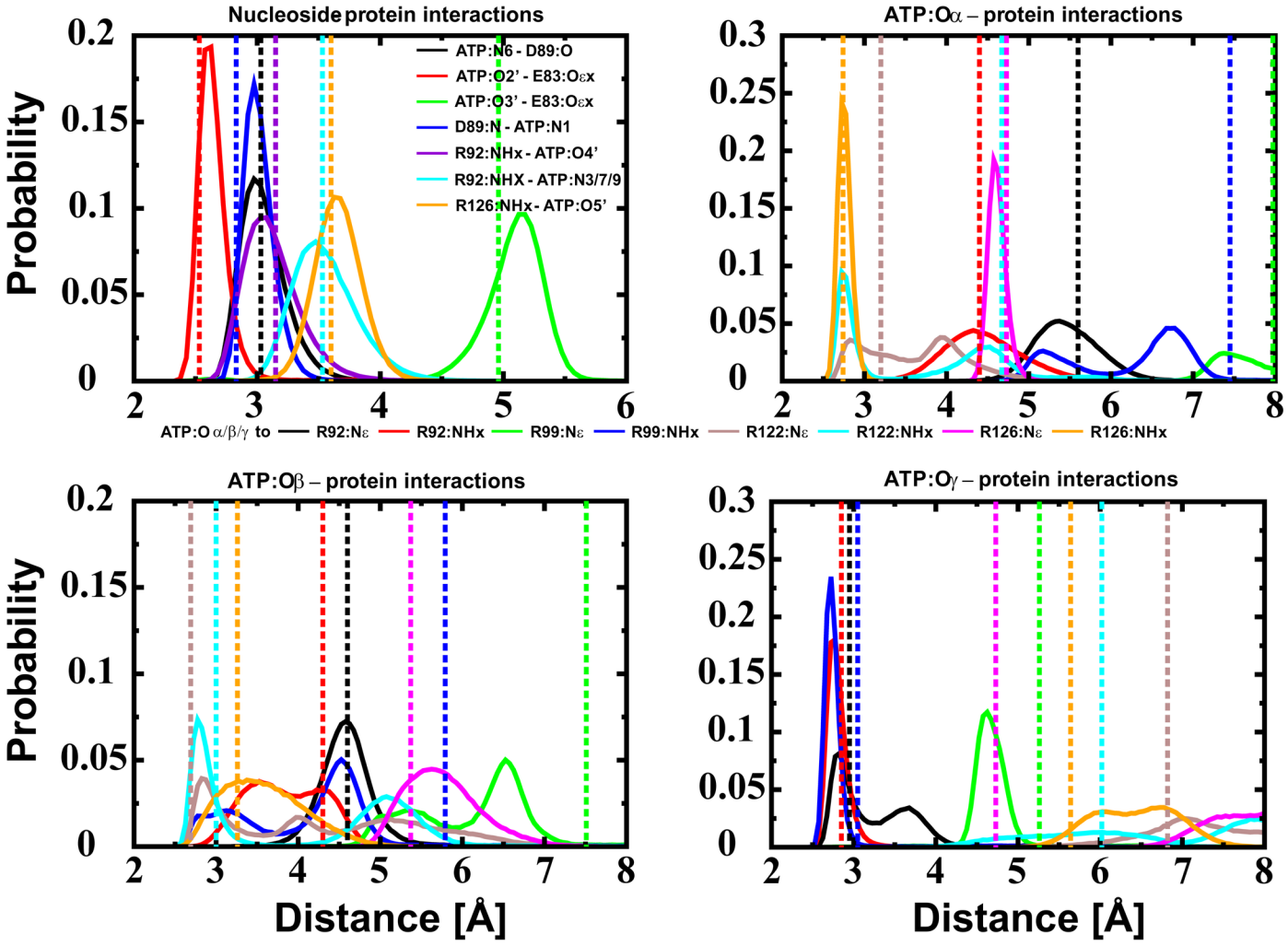

Fig 3. Distance distribution of protein-ATP interactions. Distance distribution of protein-ATP interactions of the Mg^{2+} bound to ATP:Oα/Oβ. Dotted lines represent distances found in the crystal structure of the wild type protein. The histogram in the top left represents nucleoside–protein interaction (black: ATP:N6 –D89:O, red: ATP:O2'–E:83:Oεx, green: ATP:O3'–E83:Oεx, blue: D89:N—ATP:N1, violet: R92:NHx—ATPO4', cyan: R92:NHx—ATP:N3/7/9 and orange: R126:NHx—ATP:O5'). The three other diagrams represent protein—ATP:Oα/β/γ interactions (black: R92:Nε, red: R92:NHx, green: R99:Nε, blue: R99:NHx, brown: R122:Nε, cyan: R122:NHx, magenta: R126:Nε and orange: R126:NHx), respectively. The corresponding figures for the Mg^{2+} freely distributed state and Mg^{2+} coordinated to ATP:Oβ/Oγ are shown in S2 and S4 Figs in the Supporting Information, respectively. The corresponding data for the single runs is shown in S5 (Mg^{2+} not bound in first sphere), S6 (Mg^{2+} bound to ATP:Oα/Oβ) and S7 Figs (Mg^{2+} bound to ATP:Oβ/Oγ), respectively.

https://doi.org/10.1371/journal.pone.0177907.g003

break of the ideal hydrogen-bond network—however additional biochemical/biophysical experiments and molecular dynamics simulations are necessary to understand the role of these residues in the ATP release mechanism. Assuming that the contribution of hydrophobic interactions and entropic factors are similar in the wild type and the mutant, we propose that fewer repulsive contacts of the double mutant induce a more stable binding site structure and enhance the ATP binding strength (Table 1). Taken together, all these data explain the remarkably increased (two orders of magnitudes) ATP binding affinity to the R103A/R115A double mutant [27] of the ε subunit from thermophilic *Bacillus* PS3 in respect to the wild type protein [22]. It should be noted that the model derived by X-ray crystallographic [24] for the wild type ATP binding site of the ε subunit from thermophilic *Bacillus* PS3 differs in its biological relevant monomeric state, likely caused by protein interactions (K114 and R115) of a second

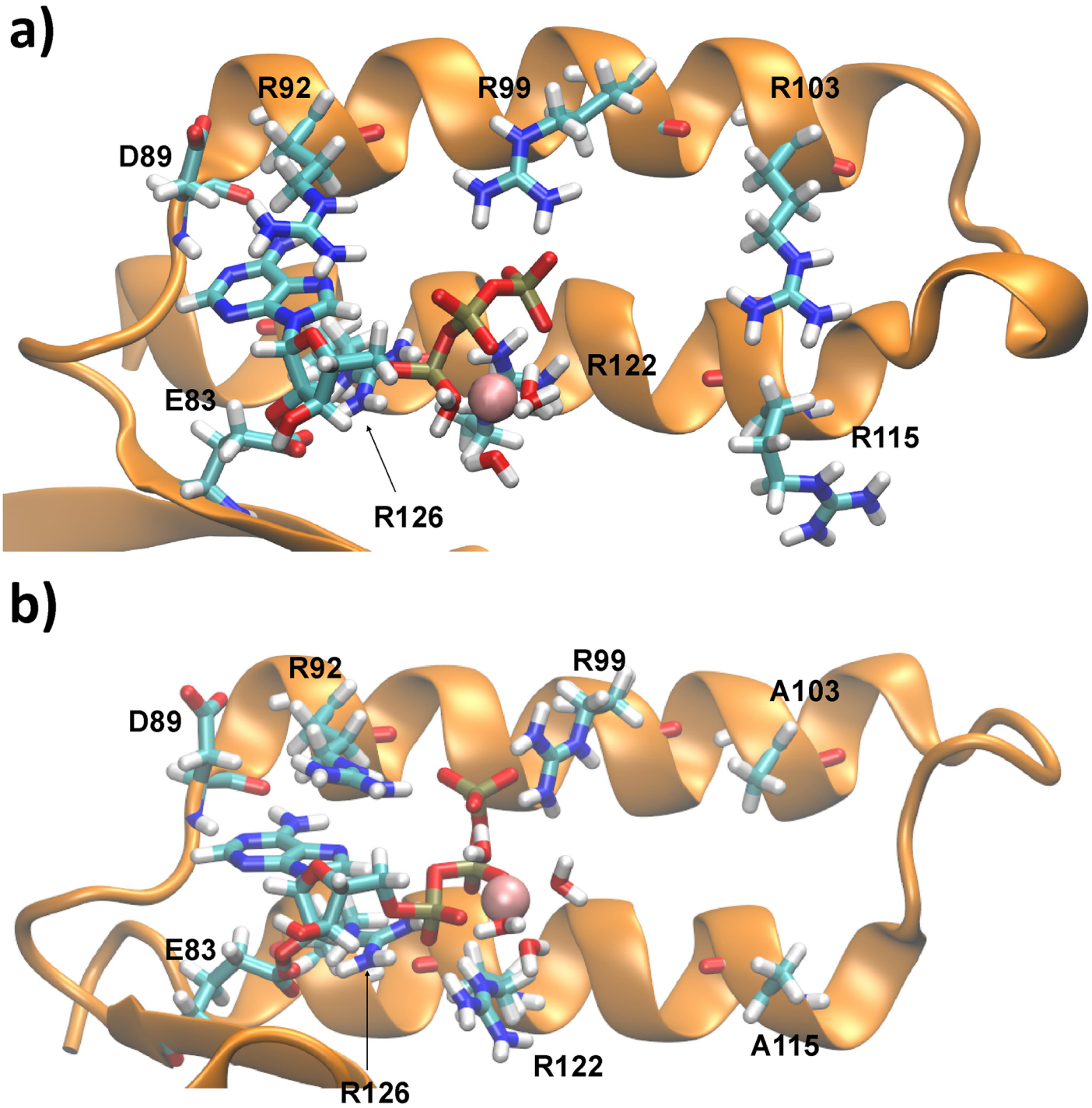

Fig 4. Comparison of wild type and mutant ATP binding site. ATP binding site of a representative snapshot of a) the wild type ε subunit [30] and b) the R103A/R115A double mutant derived by MD simulations. A structural comparison of the crystal structure and the R103A/R115A mutant is shown in the supporting information (S8 Fig). Figures containing molecular information have been produced using VMD [58].

https://doi.org/10.1371/journal.pone.0177907.g004

monomer binding to ATP of the first monomer [30]. However, the R103A/R115A mutant shows a similar binding network towards the nucleoside and phosphate group, as observed in the experimentally derived dimeric crystal structure [24], and thus represents the binding site as found in the experimentally derived structure. However, changes in the conformations of

R99 and R122 can be observed. These differences are most likely caused by the presence of unfavourable protein—protein interactions in the homodimer between positively charged residues in chain A and B; newly defined interactions between R99 and R122 towards the phosphate group, repulsive interactions between K114 and/or R115 or crystal packing effects might change the conformations of R92 and R99 in the crystal structure. A structural comparison of the R103A/R115A double mutant and the wild type crystal structure of the ε subunit from thermophilic *Bacillus* PS3 is shown in S8 Fig. The charge balance is slightly changed in the R103A/R115A mutant by an Mg^{2+} ion (interacting with two phosphate oxygen atoms) bound between ATP:Oα/Oβ and the reorientation of R99 and R122, substituting the interactions with K114 and R115 as observed in the wild type homodimer.

It has been shown previously that the ε subunit from bacterial ATP synthases can be used to sense physiological ATP concentrations in real time [32–34]. ATP binds with a two orders of magnitude decreased affinity to the wild type ε subunit from thermophilic *Bacillus* PS3 (4.3 μM) [22] in respect to the R103A/R115A double mutant (52 nM) [27]. The structural basis of high affinity ATP binding to the R103A/R115A double mutant, induced by an enhanced hydrogen bond network and reduced repulsive contacts, as discussed in this study, may allow to design novel nucleotide sensors, as e.g. AMP or ADP sensors, based on the ε subunit from bacterial ATP synthases. Introducing site directed mutations to the ATP binding site and its vicinity, taking into account the protein-ligand coordination, protein-protein interactions and repulsive contacts may help to predict/design these sensors.

Supporting information

S1 Fig. In a) the structure of the whole ε subunit from *Caldalkalibacillus thermarum* is shown. In b) the ATP binding site of the same ε subunit is highlighted. ATP is coordinated by E83, D89, R92, R99, R123 and R127. Interactions with I103 and R116 cannot be observed in the crystal structure (PDB-ID: 5HKK).
(TIF)

S2 Fig. Distance distribution of protein-ATP interactions of the ε subunit of the R103A/R115A double mutant from thermophilic *Bacillus* PS3 when the Mg^{2+} ion is freely distributed, not being bound to ATP in a first sphere coordination. Dotted lines represent distances found in the crystal structure of the wild type protein. The histogram in the top left represents nucleoside–protein interaction (black: ATP:N6 –D89:O, red: ATP:O2'–E:83:Oεx, green: ATP:O3'–E83:Oεx, blue: D89:N—ATP:N1, violet: R92:NHx—ATPO4', cyan: R92:NHx—ATP:N3/7/9 and orange: R126:NHx—ATP:O5'). The three other histograms represent protein—ATP:Oα/β/γ interactions (black: R92:Nε, red: R92:NHx, green: R99:Nε, blue: R99:NHx, brown: R122:Nε, cyan: R122:NHx, magenta: R126:Nε and orange: R126:NHx), respectively.
(TIF)

S3 Fig. Convergence of the free energy results. The solvation free energies of the Mg^{2+} ion bound in a second sphere coordination to ATP(blue), bound to ATP:Oα/Oβ (orange) and ATP:Oβ/Oγ (grey) for different time ensembles is shown. The calculated free energy differences and the standard deviation is similar in all three time ensembles. All calculations were carried out for the protein-ATP complex.
(TIF)

S4 Fig. Distance distribution of protein-ATP interactions for the R103A/R115A mutant of the ε subunit from thermophilic *Bacillus* PS3, when the Mg^{2+} ion is bound to ATP:Oβ/Oγ. Dotted lines represent distances found in the crystal structure of the wild type protein. The histogram in the top left represents nucleoside–protein interaction (black: ATP:N6 –D89:O, red:

ATP:O2'–E:83:Oεx, green: ATP:O3'–E83:Oεx, blue: D89:N—ATP:N1, violet: R92:NHx—ATPO4', cyan: R92:NHx—ATP:N3/7/9 and orange: R126:NHx—ATP:O5'). The three other histograms represent protein—ATP:Oα/β/γ interactions (black: R92:Nε, red: R92:NHx, green: R99:Nε, blue: R99:NHx, brown: R122:Nε, cyan: R122:NHx, magenta: R126:Nε and orange: R126:NHx), respectively.
(TIF)

S5 Fig. Distance distribution of protein-ATP interactions of the ε subunit of the R103A/R115A double mutant from thermophilic *Bacillus* PS3 when the Mg^{2+} ion is freely distributed, not being bound to ATP in a first sphere coordination for all three individual runs. Dotted lines represent distances found in the crystal structure of the wild type protein. The histogram in the top left represents nucleoside–protein interaction (black: ATP:N6 –D89:O, red: ATP:O2'–E:83:Oεx, green: ATP:O3'–E83:Oεx, blue: D89:N—ATP:N1, violet: R92:NHx—ATPO4', cyan: R92:NHx—ATP:N3/7/9 and orange: R126:NHx—ATP:O5'). The three other histograms represent protein—ATP:Oα/β/γ interactions (black: R92:Nε, red: R92:NHx, green: R99:Nε, blue: R99:NHx, brown: R122:Nε, cyan: R122:NHx, magenta: R126:Nε and orange: R126:NHx), respectively.
(TIF)

S6 Fig. Distance distribution of protein-ATP interactions of the ε subunit of the R103A/R115A double mutant from thermophilic *Bacillus* PS3 when the Mg^{2+} ion coordinated by ATP:Oα/Oβ in a first sphere for all three individual runs. Dotted lines represent distances found in the crystal structure of the wild type protein. The histogram in the top left represents nucleoside–protein interaction (black: ATP:N6 –D89:O, red: ATP:O2'–E:83:Oεx, green: ATP:O3'–E83:Oεx, blue: D89:N—ATP:N1, violet: R92:NHx—ATPO4', cyan: R92:NHx—ATP:N3/7/9 and orange: R126:NHx—ATP:O5'). The three other histograms represent protein—ATP:Oα/β/γ interactions (black: R92:Nε, red: R92:NHx, green: R99:Nε, blue: R99:NHx, brown: R122:Nε, cyan: R122:NHx, magenta: R126:Nε and orange: R126:NHx), respectively.
(TIF)

S7 Fig. Distance distribution of protein-ATP interactions of the ε subunit of the R103A/R115A double mutant from thermophilic *Bacillus* PS3 when the Mg^{2+} ion is coordinated by ATP:Oβ/Oγ in a first sphere for all three individual runs. Dotted lines represent distances found in the crystal structure of the wild type protein. The histogram in the top left represents nucleoside–protein interaction (black: ATP:N6 –D89:O, red: ATP:O2'–E:83:Oεx, green: ATP:O3'–E83:Oεx, blue: D89:N—ATP:N1, violet: R92:NHx—ATPO4', cyan: R92:NHx—ATP:N3/7/9 and orange: R126:NHx—ATP:O5'). The three other histograms represent protein—ATP:Oα/β/γ interactions (black: R92:Nε, red: R92:NHx, green: R99:Nε, blue: R99:NHx, brown: R122:Nε, cyan: R122:NHx, magenta: R126:N≈ and orange: R126:NHx), respectively.
(TIF)

S8 Fig. a) ATP binding site of the dimeric wild type ε subunit derived from the crystal structure (PDB-ID: 2E5Y), where ATP (chain A) is coordinated by K114 and R115 from chain B. b) ATP binding site of the R103A/R115A mutant derived from simulations. c) Aligned structure of the ATP binding site of the ε subunit from thermophilic *Bacillus* PS3 wild type (monomer A and B are shown in blue and red, respectively), as resolved in the crystal structure, and the R103A/R115A mutant (orange). The corresponding ATP molecules are coloured green (wild type) and violet (R103A/R115A mutant). The Mg^{2+} ion (R103A/R115A mutant) is shown in van der Waals spheres. Water molecules are omitted for clarity.
(TIF)

Acknowledgments

We would like to thank Ulrich Zachariae (University of Dundee) for helpful discussions.

Author Contributions

Conceptualization: AK.

Formal analysis: AK.

Funding acquisition: AK ST.

Investigation: AK.

Methodology: AK.

Project administration: AK ST.

Resources: YKY ST.

Supervision: ST.

Visualization: AK.

Writing – original draft: AK.

Writing – review & editing: AK YKY ST.

References

1. Diez M, Zimmermann B, Börsch M, König M, Schweinberger E, Steigmiller S, et al. Proton-powered subunit rotation in single membrane-bound F0F1-ATP synthase. Nat Struct Mol Biol. 2004; 11: 135–41. https://doi.org/10.1038/nsmb718 PMID: 14730350
2. Mitchell P. Coupling of phosphorylation to electron and hydrogen transfer by a chemi-osmotic type of mechanism. Nature. 1961; 191: 144–8. Available: http://www.ncbi.nlm.nih.gov/pubmed/13771349 PMID: 13771349
3. Dimroth P. Primary sodium ion translocating enzymes. Biochim Biophys Acta. 1997; 1318: 11–51. https://doi.org/10.1016/S0005-2728(96)00127-2 PMID: 9030254
4. Krah A, Pogoryelov D, Langer JD, Bond PJ, Meier T, Faraldo-Gómez JD. Structural and energetic basis for H+ versus Na+ binding selectivity in ATP synthase Fo rotors. Biochim Biophys Acta—Bioenerg. 2010; 1797: 763–772. https://doi.org/10.1016/j.bbabio.2010.04.014 PMID: 20416273
5. Noji H, Yasuda R, Yoshida M, Kinosita K. Direct observation of the rotation of F1-ATPase. Nature. 1997; 386: 299–302. https://doi.org/10.1038/386299a0 PMID: 9069291
6. Drobinskaya IY, Kozlov IA, Murataliev MB, Vulfson EN. Tightly bound adenosine diphosphate, which inhibits the activity of mitochondrial F1-ATPase, is located at the catalytic site of the enzyme. FEBS Lett. 1985; 182: 419–424. https://doi.org/10.1016/0014-5793(85)80346-X PMID: 2858407
7. Hyndman DJ, Milgrom YM, Bramhall EA, Cross RL. Nucleotide-binding sites on Escherichia coli F1-ATPase. Specificity of noncatalytic sites and inhibition at catalytic sites by MgADP. J Biol Chem. 1994; 269: 28871–7. Available: http://www.ncbi.nlm.nih.gov/pubmed/7961847 PMID: 7961847
8. Hirono-Hara Y, Noji H, Nishiura M, Muneyuki E, Hara KY, Yasuda R, et al. Pause and rotation of F(1)-ATPase during catalysis. Proc Natl Acad Sci U S A. 2001; 98: 13649–54. https://doi.org/10.1073/pnas.241365698 PMID: 11707579
9. Pullman ME, Monroy GC. A NATURALLY OCCURRING INHIBITOR OF MITOCHONDRIAL ADENOSINE TRIPHOSPHATASE. J Biol Chem. 1963; 238: 3762–9. Available: http://www.ncbi.nlm.nih.gov/pubmed/14109217 PMID: 14109217
10. Cabezon E, Butler PJG, Runswick MJ, Walker JE. Modulation of the Oligomerization State of the Bovine F1-ATPase Inhibitor Protein, IF1, by pH. J Biol Chem. 2000; 275: 25460–25464. https://doi.org/10.1074/jbc.M003859200 PMID: 10831597
11. Cabezón E, Runswick MJ, Leslie AG, Walker JE. The structure of bovine IF(1), the regulatory subunit of mitochondrial F-ATPase. EMBO J. 2001; 20: 6990–6. https://doi.org/10.1093/emboj/20.24.6990 PMID: 11742976

12. Cabezón E, Arechaga I, Jonathan P, Butler G, Walker JE. Dimerization of bovine F1-ATPase by binding the inhibitor protein, IF1. J Biol Chem. 2000; 275: 28353–5. https://doi.org/10.1074/jbc.C000427200 PMID: 10918052

13. Tsunoda SP, Rodgers AJ, Aggeler R, Wilce MC, Yoshida M, Capaldi RA. Large conformational changes of the epsilon subunit in the bacterial F1F0 ATP synthase provide a ratchet action to regulate this rotary motor enzyme. Proc Natl Acad Sci U S A. National Academy of Sciences; 2001; 98: 6560–4. https://doi.org/10.1073/pnas.111128098 PMID: 11381110

14. Suzuki T, Murakami T, Iino R, Suzuki J, Ono S, Shirakihara Y, et al. F0F1-ATPase/synthase is geared to the synthesis mode by conformational rearrangement of epsilon subunit in response to proton motive force and ADP/ATP balance. J Biol Chem. 2003; 278: 46840–6. https://doi.org/10.1074/jbc.M307165200 PMID: 12881515

15. Feniouk BA, Kato-Yamada Y, Yoshida M, Suzuki T. Conformational transitions of subunit epsilon in ATP synthase from thermophilic bacillus PS3. Biophys J. 2010; 98: 434–442. https://doi.org/10.1016/j.bpj.2009.10.023 PMID: 20141757

16. Cingolani G, Duncan TM. Structure of the ATP synthase catalytic complex (F(1)) from Escherichia coli in an autoinhibited conformation. Nat Struct Mol Biol. 2011; 18: 701–7. https://doi.org/10.1038/nsmb.2058 PMID: 21602818

17. Shirakihara Y, Shiratori A, Tanikawa H, Nakasako M, Yoshida M, Suzuki T. Structure of a thermophilic F1-ATPase inhibited by an ε-subunit: deeper insight into the ε-inhibition mechanism. FEBS J. 2015; 282: 2895–913. https://doi.org/10.1111/febs.13329 PMID: 26032434

18. Sobti M, Smits C, Wong AS, Ishmukhametov R, Stock D, Sandin S, et al. Cryo-EM structures of the autoinhibited E. coli ATP synthase in three rotational states. Elife. 2016; 5: e21598. https://doi.org/10.7554/eLife.21598 PMID: 28001127

19. Iino R, Hasegawa R, Tabata K V, Noji H. Mechanism of inhibition by C-terminal alpha-helices of the epsilon subunit of Escherichia coli FoF1-ATP synthase. J Biol Chem. 2009; 284: 17457–64. https://doi.org/10.1074/jbc.M109.003798 PMID: 19411254

20. Krah A. Linking structural features from mitochondrial and bacterial F-type ATP synthases to their distinct mechanisms of ATPase inhibition. Prog Biophys Mol Biol. 2015; 119: 94–102. https://doi.org/10.1016/j.pbiomolbio.2015.06.005 PMID: 26140992

21. Kato-Yamada Y, Yoshida M. Isolated epsilon subunit of thermophilic F1-ATPase binds ATP. J Biol Chem. 2003; 278: 36013–36016. https://doi.org/10.1074/jbc.M306140200 PMID: 12837747

22. Kato S, Yoshida M, Kato-Yamada Y. Role of the ϵ Subunit of Thermophilic F1-ATPase as a Sensor for ATP. J Biol Chem. 2007; 282: 37618–37623. https://doi.org/10.1074/jbc.M707509200 PMID: 17933866

23. Kato-Yamada Y. Isolated ε subunit of Bacillus subtilis F1-ATPase binds ATP. FEBS Lett. 2005; 579: 6875–6878. https://doi.org/10.1016/j.febslet.2005.11.036 PMID: 16337201

24. Yagi H, Kajiwara N, Tanaka H, Tsukihara T, Kato-Yamada Y, Yoshida M, et al. Structures of the thermophilic F1-ATPase subunit suggesting ATP-regulated arm motion of its C-terminal domain in F1. Proc Natl Acad Sci U S A. 2007; 104: 11233–11238. https://doi.org/10.1073/pnas.0701045104 PMID: 17581881

25. Uhlin U, Cox GB, Guss JM. Crystal structure of the epsilon subunit of the proton-translocating ATP synthase from Escherichia coli. Structure. 1997; 5: 1219–30. https://doi.org/10.1016/s0969-2126(97)00272-4 PMID: 9331422

26. Krah A, Takada S. On the Mg2+ binding site of the ε subunit from bacterial F-type ATP synthases. Biochim Biophys Acta—Bioenerg. 2015; 1847: 1101–1112. Available: http://www.ncbi.nlm.nih.gov/pubmed/26028301

27. Kato-Yamada Y. High affinity nucleotide-binding mutant of the ε subunit of thermophilic F1-ATPase. Biochem Biophys Res Commun. 2016; 469: 1129–1132. https://doi.org/10.1016/j.bbrc.2015.12.121 PMID: 26746006

28. Yagi H, Konno H, Murakami-Fuse T, Isu A, Oroguchi T, Akutsu H, et al. Structural and functional analysis of the intrinsic inhibitor subunit ϵ of F 1 -ATPase from photosynthetic organisms. Biochem J. 2010; 425: 85–98. https://doi.org/10.1042/BJ20091247 PMID: 19785575

29. Wilkens S, Dahlquist FW, McIntosh LP, Donaldson LW, Capaldi RA. Structural features of the ε subunit of the Escherichia coli ATP synthase determined by NMR spectroscopy. Nat Struct Biol. 1995; 2: 961–967. https://doi.org/10.1038/nsb1195-961 PMID: 7583669

30. Krah A, Takada S. On the ATP binding site of the ε subunit from bacterial F-type ATP synthases. Biochim Biophys Acta—Bioenerg. 2016; 1857: 332–340. https://doi.org/10.1016/j.bbabio.2016.01.007 PMID: 26780667

31. Ferguson SA, Cook GM, Montgomery MG, Leslie AGW, Walker JE. Regulation of the thermoalkaliphilic F1-ATPase from Caldalkalibacillus thermarum. Proc Natl Acad Sci U S A. 2016; 113: 10860–5. https://doi.org/10.1073/pnas.1612035113 PMID: 27621435

32. Imamura H, Nhat KPH, Togawa H, Saito K, Iino R, Kato-Yamada Y, et al. Visualization of ATP levels inside single living cells with fluorescence resonance energy transfer-based genetically encoded indicators. Proc Natl Acad Sci U S A. 2009; 106: 15651–6. https://doi.org/10.1073/pnas.0904764106 PMID: 19720993

33. Yaginuma H, Kawai S, Tabata K V, Tomiyama K, Kakizuka A, Komatsuzaki T, et al. Diversity in ATP concentrations in a single bacterial cell population revealed by quantitative single-cell imaging. Sci Rep. 2014; 4: 6522. https://doi.org/10.1038/srep06522 PMID: 25283467

34. Yoshida T, Kakizuka A, Imamura H. BTeam, a Novel BRET-based Biosensor for the Accurate Quantification of ATP Concentration within Living Cells. Sci Rep. 2016; 6: 39618. https://doi.org/10.1038/srep39618 PMID: 28000761

35. Kioka H, Kato H, Fujikawa M, Tsukamoto O, Suzuki T, Imamura H, et al. Evaluation of intramitochondrial ATP levels identifies G0/G1 switch gene 2 as a positive regulator of oxidative phosphorylation. Proc Natl Acad Sci U S A. 2014; 111: 273–8. https://doi.org/10.1073/pnas.1318547111 PMID: 24344269

36. Hatsugai N, Perez Koldenkova V, Imamura H, Noji H, Nagai T. Changes in cytosolic ATP levels and intracellular morphology during bacteria-induced hypersensitive cell death as revealed by real-time fluorescence microscopy imaging. Plant Cell Physiol. 2012; 53: 1768–75. https://doi.org/10.1093/pcp/pcs119 PMID: 22942251

37. Ando T, Imamura H, Suzuki R, Aizaki H, Watanabe T, Wakita T, et al. Visualization and measurement of ATP levels in living cells replicating hepatitis C virus genome RNA. PLoS Pathog. 2012; 8: e1002561. https://doi.org/10.1371/journal.ppat.1002561 PMID: 22396648

38. Hollopeter G, Jantzen HM, Vincent D, Li G, England L, Ramakrishnan V, et al. Identification of the platelet ADP receptor targeted by antithrombotic drugs. Nature. 2001; 409: 202–7. https://doi.org/10.1038/35051599 PMID: 11196645

39. Cheung PC, Salt IP, Davies SP, Hardie DG, Carling D. Characterization of AMP-activated protein kinase gamma-subunit isoforms and their role in AMP binding. Biochem J. 2000; 346: 659–69. PMID: 10698692

40. Pronk S, Pall S, Schulz R, Larsson P, Bjelkmar P, Apostolov R, et al. GROMACS 4.5: a high-throughput and highly parallel open source molecular simulation toolkit. Bioinformatics. 2013; 29: 845–854. https://doi.org/10.1093/bioinformatics/btt055 PMID: 23407358

41. Cornell WD, Cieplak P, Bayly CI, Gould IR, Merz KM, Ferguson DM, et al. A Second Generation Force Field for the Simulation of Proteins, Nucleic Acids, and Organic Molecules. J Am Chem Soc. 1995; 117: 5179–5197. https://doi.org/10.1021/ja00124a002

42. Wang J, Cieplak P, Kollman PA. How well does a restrained electrostatic potential (RESP) model perform in calculating conformational energies of organic and biological molecules? J Comput Chem. 2000; 21: 1049–1074. https://doi.org/10.1002/1096-987X(200009)21:12<1049::AID-JCC3>3.0.CO;2-F

43. Meagher KL, Redman LT, Carlson HA. Development of polyphosphate parameters for use with the AMBER force field. J Comput Chem. 2003; 24: 1016–1025. https://doi.org/10.1002/jcc.10262 PMID: 12759902

44. Hornak V, Abel R, Okur A, Strockbine B, Roitberg A, Simmerling C. Comparison of multiple Amber force fields and development of improved protein backbone parameters. Proteins Struct Funct Bioinforma. 2006; 65: 712–725. https://doi.org/10.1002/prot.21123 PMID: 16981200

45. Lindorff-Larsen K, Piana S, Palmo K, Maragakis P, Klepeis JL, Dror RO, et al. Improved side-chain torsion potentials for the Amber ff99SB protein force field. Proteins Struct Funct Bioinforma. 2010; 78: 1950–1958. https://doi.org/10.1002/prot.22711 PMID: 20408171

46. Sorin EJ, Pande VS. Exploring the Helix-Coil Transition via All-Atom Equilibrium Ensemble Simulations. Biophys J. 2005; 88: 2472–2493. https://doi.org/10.1529/biophysj.104.051938 PMID: 15665128

47. Åqvist J. Ion-water interaction potentials derived from free energy perturbation simulations. J Phys Chem. 1990; 94: 8021–8024. https://doi.org/10.1021/j100384a009

48. Parrinello M, Rahman A. Polymorphic transitions in single crystals: A new molecular dynamics method. J Appl Phys. 1981; 52: 7182–7190. https://doi.org/10.1063/1.328693

49. Bussi G, Donadio D, Parrinello M. Canonical sampling through velocity rescaling. J Chem Phys. 2007; 126: 14101. https://doi.org/10.1063/1.2408420 PMID: 17212484

50. Darden T, York D, Pedersen L. Particle mesh Ewald: An N ·log (N) method for Ewald sums in large systems. J Chem Phys. 1993; 98: 10089–10092. https://doi.org/10.1063/1.464397

51. Bennett CH. Efficient estimation of free energy differences from Monte Carlo data. J Comput Phys. 1976; 22: 245–268. https://doi.org/10.1016/0021-9991(76)90078-4

52. Srinivasan J, Cheatham TE, Cieplak P, Kollman PA, Case DA. Continuum Solvent Studies of the Stability of DNA, RNA, and Phosphoramidate–DNA Helices. J Am Chem Soc. 1998; 120: 9401–9409. https://doi.org/10.1021/JA981844

53. Kumari R, Kumar R, Lynn A. g_mmpbsa—A GROMACS Tool for High-Throughput MM-PBSA Calculations. J Chem Inf Model. 2014; 54: 1951–1962. https://doi.org/10.1021/ci500020m PMID: 24850022

54. Baker NA, Sept D, Joseph S, Holst MJ, McCammon JA. Electrostatics of nanosystems: Application to microtubules and the ribosome. Proc Natl Acad Sci U S A. 2001; 98: 10037–10041. https://doi.org/10.1073/pnas.181342398 PMID: 11517324

55. Sharp KA, Honig B. Calculating total electrostatic energies with the nonlinear Poisson-Boltzmann equation. J Phys Chem. 1990; 94: 7684–7692. https://doi.org/10.1021/j100382a068

56. Espinosa E, Molins E, Lecomte C. Hydrogen bond strengths revealed by topological analyses of experimentally observed electron densities. Chem Phys Lett. 1998; 285: 170–173.

57. Homeyer N, Stoll F, Hillisch A, Gohlke H. Binding Free Energy Calculations for Lead Optimization: Assessment of Their Accuracy in an Industrial Drug Design Context. J Chem Theory Comput. 2014; 10: 3331–3344. https://doi.org/10.1021/ct5000296 PMID: 26588302

58. Humphrey W, Dalke A, Schulten K. VMD: visual molecular dynamics. J Mol Graph. 1996; 14: 33–8, 27–8. Available: http://www.ncbi.nlm.nih.gov/pubmed/8744570 PMID: 8744570